LAWRENCE
LIVERMORE
NATIONAL
LABORATORY

UCRL-JRNL-207203

Simulating thermal explosion of RDX-based explosives: Model comparison with experiment

J. J. Yoh, M. A. McClelland, J. L. Maienschein, J. F. Wardell, C. M. Tarver

October 13, 2004

Journal of Applied Physics

Disclaimer

Simulating thermal explosion of RDX-based explosives: Model comparison with experiment

Jack J. Yoh,* Matthew A. McClelland, Jon L. Maienschein, Jeffrey F. Wardell, and Craig M. Tarver

Energetic Materials Center

Lawrence Livermore National Laboratory,

Livermore, CA 94551

A manuscript submitted to the *Journal of Applied Physics*

(Dated: October 8, 2004)

Abstract

We compare two-dimensional model results with measurements for the thermal, chemical and mechanical behavior in a thermal explosion experiment. Confined high explosives are heated at a rate of 1 °C per hour until an explosion is observed. The heating, ignition, and deflagration phases are modeled using an Arbitrarily Lagrangian-Eulerian code (ALE3D) that can handle a wide range of time scales that vary from a structural to a dynamic hydro time scale. During the pre-ignition phase, quasi-static mechanics and diffusive thermal transfer from a heat source to the HE are coupled with the finite chemical reactions that include both endothermic and exothermic processes. Once the HE ignites, a hydro dynamic calculation is performed as a burn front propagates through the HE. Two RDX-based explosives, C-4 and PBXN-109, are considered, whose chemical-thermal-mechanical models are constructed based on measurements of thermal and mechanical properties along with small scale thermal explosion measurements. The simulated dynamic response of HE confinement during the explosive phase is compared to measurements in larger scale thermal explosion tests. The explosion temperatures for both HE's are predicted to within 5 °C. Calculated and measured wall strains provide an indication of vessel pressurization during the heating phase and violence during the explosive phase. During the heating phase, simulated wall strains provide only an approximate representation of measured values indicating a better numerical treatment is needed to provide accurate results. The results also show that more numerical accuracy is needed for vessels with lesser confinement strength. For PBXN-109, the measured wall strains during the explosion are well represented by the ALE3D calculations.

PACS numbers:

*Electronic address: yoh1@llnl.gov

I. INTRODUCTION

In the DoD/DOE community, there is an interest in using computer simulations to reduce the number of experiments for weapons design and safety evaluation. One area of success in modeling and simulation is the characterization of munitions exposed to extreme conditions, such as shocks and detonations [1–3]. Hydrocodes, which are designed to simulate the high-frequency response involving initiation and propagation of shocks and detonations, have been used extensively by the energetic materials community [4–10].

On the other hand, models and numerical strategies are still being developed for the heating of energetic materials until reaction (cookoff) [11–18]. The Navy is interested in the behavior of munitions in shipboard fires to help with the design of storage systems and the development of fire fighting strategies. In these fires, time scales for behavior can range from days to microseconds. During the relatively slow heating phase, the response of an energetic materials system is paced by thermal diffusion and chemical decomposition, while the mechanical response is essentially a quasi-static process. As the decomposition reactions accelerate, heat is generated faster than it can diffuse. Product gases are formed and the resulting pressure rises accelerate the energetic and containment material response. The resulting thermal explosion can range in violence from a pressure rupture to a detonation.

A number of investigators have modeled slow cookoff experiments. Chidester *et al.* [19] calculated explosion times for HMX- and TATB-based explosives subjected to varying confinement and thermal environments. Tarver and Tran [20] improved thermal decomposition models for HMX-based plastic bonded explosives and attained reasonable predictions for ignition time using the thermal-chemical code, Chemical TOPAZ. These thermo-chemical models were expanded to include hydro effects, and the earlier models were evaluated against small-scale tests (see [15, 21–23]). It was recognized that the models required further development and needed to be benchmarked against well-instrumented cookoff experiments (see [14, 24, 25]). More recent modeling efforts have focused on wall strain rates as a measure of cookoff violence. Erikson *et al.* [26] used a suite of codes to model the two separate phases of the cookoff process. The information obtained from their pre-ignition calculation was used to initialize the post-ignition simulation for predicting the wall expansion.

In the modeling work of this study, the process of cookoff is not separated into two regimes. Instead, a single calculation is performed for the heating, ignition, and explosive

phases of cookoff. Coupled thermal, mechanical, and chemical models are used during all of these stages to account for effects such as chemical decomposition, burning, thermal expansion, and the closing of gaps. It is seen that the modeling of thermal explosions requires computational tools and models that can handle a wide variety of physical processes and time scales.

We consider the explosives C-4 and PBXN-109 which have an RDX (cyclonite) base[27]. The C-4 has a nominal composition of 91% RDX, 7% Fuel Oil, and 2% PIB (polyisobutylene) by weight, and the composition of PBXN-109 is 64% RDX, 20% Al, and 16% DOA (dioctyl adipate)/HTPB (hydroxy terminate polybutadiene) binder. Because of the relatively low content of RDX and the presence of an inactive binder, PBXN-109 is an insensitive high explosive. The selection of these explosives allows us to investigate a range of RDX contents with simulations and experiments.

In this paper, we investigate the response of confined RDX-based materials in our Scaled Thermal Explosion Experiment (STEX). We use our ALE3D models to calculate temperature fields, the time to explosion, and strain of the vessel wall during the heating, ignition, and explosive phases of the experiment. A numerical approach involving variable mass-scaling allows the calculation of coupled thermo-chemical-mechanical results over the widely varying time scales associated with the heating and explosive processes [28, 29]. In all cases, we have performed mesh refinement analysis to help assess the accuracy of the results. Model simulations are compared with measurements from thermocouples and strain gauges.

II. SCALE THERMAL EXPLOSION EXPERIMENT (STEX)

In order to provide a database to test models, the STEX is designed to quantify the violence of thermal explosions under carefully controlled conditions[14]. The cylindrical test, shown in Fig. 1, is designed to provide ignition in the central region of the cylinder. The confinement vessel consists of a 4130 steel tube with heavily reinforced end caps which confine the decomposition gases until the tube wall fails. A length to diameter ratio of 4:1 is used for which the ID is 5.08 cm and the interior length is 20.3 cm. In this paper we model the results for STEX test TE-040 for C-4 and test no. TE-036 for PBXN-109. Two different wall thicknesses were used. First, the wall thickness for PBXN-109 was 0.4 cm, giving an approximate confinement pressure of 200 MPa. As for C-4, we used 0.1 cm thick wall, giving

an approximate confinement pressure of 50 MPa. Ullage (air space) was included to allow for expansion of the HE without bursting the vessel prior to ignition. The total ullage that is present in the vessel was 5% for PBXN-109 and 6% for C-4. The ullage on the side of the HE is 1% for PBXN-109 and 3% for C-4.

A feedback control system is used to adjust three radiant heaters to control the wall temperature at location no. 1 of Fig. 1(b). The thermocouples at location nos. 2 and 3 on the end caps are controlled with separate control loops. The wall thermocouple temperature is increased at 1 ^{o}C/h until explosion. The lower and upper thermocouples are maintained at 4 and 9 ^{o}C, respectively, below the wall temperature to provide for ignition near a plane half way between the two end caps. A probe with 5 thermocouples is used to monitor the internal temperature of the HE (see Fig. 1(b)). Two hoop strain gauges were used to measure the radial expansion of the tube at the axial midplane.

III. MODELS FOR RDX-BASED EXPLOSIVES

In this model, the solid explosive decomposes volumetrically as it is heated to generate product gases (see Fig. 2(a)). These reactions accelerate to a point at which the HE ignites and burns. A burn front then moves as a sheet away from the ignition point (see Fig. 2(b)). Partially decomposed HE is converted to products as the burn front propagates. The product gases pressurize the vessel and drive the wall outward.

The decomposition of the two RDX-based explosives is modeled by three-step, four-species chemical kinetics based on the pure RDX model reported in [30]. The mechanical models for the solid chemical constituents along with the steel components are taken to have Steinberg-Guinan [31] strength models in which a polynomial expression is used for the equations of state. The gaseous products are treated as no-strength materials with gamma-law equations of state. The thermal conductivity for the HE solid species is taken to be constant, whereas the effects of temperature are included for the gaseous species. The air in the gaps between the HE and the steel case is described with a gamma-law model.

A. Chemical model

The three-step, four-species reaction mechanism for C-4 is

$$\mathrm{A} \rightarrow \mathrm{B}, \quad r_1 = Z_1 \exp(-E_1/RT)\, \rho_{\mathrm{A}} \tag{1}$$

$$\mathrm{B} \rightarrow \mathrm{C}, \quad r_2 = Z_2 \exp(-E_2/RT)\, \rho_{\mathrm{B}} \tag{2}$$

$$\mathrm{C} \rightarrow \mathrm{D}, \quad r_3 = Z_3 \exp(-E_3/RT)\, \rho_{\mathrm{C}}^2 \tag{3}$$

where A and B are solid species, and C and D are product gases. Here r_i is the mass reaction rate, Z_i is the frequency factor, and E_i is the activation energy for reaction i. Also ρ_j is the mass concentration for species $j = A, B, C, D$. The mechanism for PBXN-109 uses a slight modification to the above standard steps; the second exothermic reaction step is replaced by the following,

$$\mathrm{B} \rightarrow \mathrm{C} + Al, \quad r_2 = Z_2 \exp(-E_2/RT)\, \rho_{\mathrm{B}} \tag{4}$$

where Al, a constituent of species B, is treated as inert. In [13], an alternative model was developed in which Al reacts to completion. Although both models can represent the available explosion, the question of Al reactivity remains. The rate parameters in the above mechanisms for C-4 and PBXN-109 are adjusted to fit One-Dimensional-Time-to-Explosion (ODTX) measurements [32]. The values are given in Tables II and I

The time-to-ignition measurements are made using a standard ODTX apparatus in which the outer surface of a 1.27 cm diameter HE sphere is suddenly increased to a specified temperature. The time to explosion is the time elapsed from the start of heating until confinement failure. The measured and calculated ODTX results for C-4 and PBXN-109 are shown in Figs. 3 and 4, respectively. The ODTX measurements for both explosives include samples from the lots of C-4 and PBXN-109 used in the larger scale STEX tests [33]. Also, shown for PBXN-109 are measurements from an earlier study. The model includes chemical reaction and thermal transport without material motion. The model provides a good description of the measurements which exhibit some scatter. The measurements for PBXN-109 are well represented by the model, except for temperatures above 235 °C (see Fig. 4).

After the chemical reactions have progressed significantly into the faster regime of cookoff in which changes are occurring on the time scale of the sound speed, a switch is made to

a burn front model in which reactants are converted completely to products in a single reaction step. The burn front velocity, V is assumed to be a pressure-dependent function, and it takes the form

$$V = a P^n \tag{5}$$

where V is in mm/s and P is in MPa.

This change in models is made for several reasons. First the Arrhenius models described above may not apply at the elevated temperatures and pressures of the burn process. The burn rate model is more useful since it can employ measured burn rates as described below. Finally, the computational effort required for the Arrhenius model is prohibitively large as a result of the fine mesh spacing and small time steps required to model the narrow burn front. In contrast, solutions for the burn rate model can be obtained with practical amounts of computation time.

The parameters used in the current simulation are:

$$a = 1.548 \text{ (mm/s} - \text{MPa}^{-n}\text{)}, \quad n = 1.02 \quad \text{(C-4)}$$
$$a = 0.146 \text{ (mm/s} - \text{MPa}^{-n}\text{)}, \quad n = 1.45 \quad \text{(PBXN-109)}$$

Fig. 5 shows two straight lines that represent the burn rate measurements. The burn rates are measured using the LLNL High Pressure Strand Burner [34]. A strand of explosive (0.64 cm D x 5.7 cm L) is placed in a high pressure vessel, and is ignited at one end. Wires placed in the sample track the progress of the burn while pressure measurements are made.

B. Constitutive model at high-strain rate

The solid chemical constituents (A, B) of model HE and the 4130 steel are taken to be Steinberg-Guinan materials that incorporate an equation of state (EOS) and expressions for the shear modulus μ and yield strength Y. The steel model includes strain hardening, while the HE is taken to be perfectly plastic above the yield point.

The expression for the EOS of the unreacted explosive follows a 7-term polynomial in the form of

$$P(\xi) = a_0 + a_1\xi + a_2\xi^2 + a_3\xi^3 + (b_0 + b_1\xi + b_2\xi^2)\rho_0 c_v(T - T_0) \tag{6}$$

where the volumetric compression is defined $\xi = \rho/\rho_0 - 1$. Thus, a single EOS is used to represent behavior involving slow heating and the explosive process.

For the HE's, we set $a_0 = b_2 = 0$ and $b_0 = b_1$. For PBXN-109, the parameters, a_1, a_2, a_3, and b_0 were adjusted using a nonlinear regression procedure to provide a best fit of the measured thermal expansion, heat capacity, temperature-dependent hydrostatic compression, and the unreacted shock Hugoniot (see [35]). All measurements are for the sample of this study, except for the shock Hugoniot. For C-4, these same parameters were adjusted to fit earlier measurements of the thermal expansion, heat capacity, sound speed, and unreacted shock Hugoniot. In some cases, these properties were constructed from constituent measurements using mixing rules.

The model chemical components (C, D) are treated as no-strength materials with gamma-law equations of state,

$$P = (\gamma - 1)\,\rho\, c_v\, T \tag{7}$$

This type of EOS provides an approximate description for the relatively low confinement pressures (< 10 kbar) of thermal explosion tests. The value γ is adjusted using a pressure of 1 kbar, a temperature of 2000 °C, and density and heat capacity c_v determined from the thermo-chemical equilibrium computer code, Cheetah 3.0 [36] for the final product gases. A summary of the adjusted parameters for the current equations of state is given in Table III.

For all of the solid materials, the shear modulus, μ, and yield stress, Y, are assumed to vary with temperature, but are not strain-rate dependent. Strain hardening is present for the steel, but not for the solid HE constituents (see Table IV).

$$\mu(P, \eta, T) = \mu_0 \left[1 + b\frac{P}{\eta^{1/3}} - h(T - 300)\right] \tag{8}$$

$$Y(P, \eta, \bar{\epsilon}^p, T) = Y_0[1 + \beta(\bar{\epsilon}^p + \bar{\epsilon}_0^p)]^n \, \frac{\mu}{\mu_0} \tag{9}$$

with the maximum work hardening given by

$$Y_0[1 + \beta(\bar{\epsilon}^p + \bar{\epsilon}_0^p)]^n \leq Y_{\max}. \tag{10}$$

In these expressions, we have

$$\eta = \frac{\rho}{\rho_0}$$

$$\bar{\epsilon}^p = \int \dot{\bar{\epsilon}}^p \, dt$$

$$\dot{\bar{\epsilon}}^p = \sqrt{\frac{2}{3}\left((\dot{\epsilon}_1^p - \dot{\epsilon}_2^p)^2 (\dot{\epsilon}_2^p - \dot{\epsilon}_3^p)^2 (\dot{\epsilon}_3^p - \dot{\epsilon}_1^p)^2\right)}$$

where the directional components of plastic strain rates are noted as $\dot{\epsilon}_i^p$. The subscript 0 refers to the reference state ($T = 300\,^{o}\mathrm{K}$, $P = 0$, $\epsilon = 0$). In general, we set $\bar{\epsilon}_0^p$ to zero for each material. When melting occurs ($T \geq T_m$), the material model assumes zero strength and effectively $\mu = Y = 0$.

In [37], the authors showed that for materials that do not exhibit strain-rate dependency, Y is expected to be proportional to μ; that is Y/μ is a constant. Generally, this ratio decreases with temperature at a rate directly related to $\dot{\epsilon}$, $\dot{\epsilon} \geq 10^5\,\mathrm{s}^{-1}$, where a weaker temperature dependence is observed.

It is important to note that μ and Y drop to zero upon melting and that the above expressions are valid for the solid phase where $T < T_m$. The melt temperature T_m is given by a modified Lindemann melting law which is given elsewhere [38].

The present strength model of Steinberg-Guinan predicts that the shear modulus decreases with temperature, dropping abruptly to zero at $T \geq T_m$. For further detail on the model, readers are referred to [37, 39].

The constants $b, h, \beta, n, \mu_0, Y_0$ and $Y_{\max}$ are shown in Table V. For PBXN-109, the values for μ_0 and Y_0 were based on measurements as described by McClelland *et al.*[11] These same values were used for C-4 as a rough approximation. It is noted that all of these parameters are much smaller than the values for steel. Since the strength of the solid HE constituents is small, the behavior is similar in many ways to that of a hydrostatic liquid. A more complex viscoelastic model would be a better choice for all of the solid HE constituents. The PBXN-109 has 16% plastic binder and the C-4 has 2% fuel oil and 7% PIB binder. These materials would be expected to exhibit viscous behavior at low strain rates during the heating phase and more elastic behavior at high strain rates. The impact of the model choices are being explored in this and other investigations.

C. Thermal model

The time-dependent thermal transport model includes the effects of conduction, reaction, convection, and compression. The constant-volume heat capacity is constant for each reactant consistent with the Steinberg-Guinan model. The thermal conductivities of the solid species A and B are taken to be constant, whereas the effects of temperature are included for the gaseous species. The thermal properties for materials A and B are listed in Table III

and use available measured values for C-4 and PBXN-109. The heat capacity, c_v, for gases C and D is assigned the same constant-volume value used in the gamma-law model. The temperature-dependent thermal conductivity is estimated at 1 kbar and T = 2000 °C using Bridgmann's equation[40] for liquids in which the sound velocity is calculated using results from Cheetah.

IV. MESHES, BOUNDARY CONDITIONS, AND NUMERICAL STRATEGY

A. One-Dimensional-Time-to-Explosion (ODTX) tests

The ODTX system is modeled using the ALE3D code; the problem is spherically symmetric and one-dimensional in the r-direction. The mesh has one row of 50 elements in the shape of a 'piton,' running from the center of the half-inch sphere to the outer boundary at $r = 0.635$ cm (see Fig. 6). The center axis of the piton is the x-axis. The vertex of the piton is flattened so that the mesh can be constructed from 8-noded hexahedral brick elements. The full domain is then a sphere with a small hole in the center. A step thermal boundary condition is applied at the outer end of the mesh. The decomposition rate accelerates and the calculation continues until the time step size decreases to a user-specified value. This time is taken to be the time to explosion.

B. Scaled Thermal Explosion test (STEX)

Fig. 7 shows one and two-dimensional modeling domains for a STEX test. A wedge slice is taken from the center line of the STEX system shown in the right image. This one-dimensional wedge represents an axisymmetric section of the STEX system in which variations occur only in the radial direction. This approach is taken to minimize the number of three-dimensional zones needed to represent an axisymmetric domain. The boundaries at two planes of constant θ and two planes of constant z are rigid slip surfaces. In the experiment [14], the HE, nominally 5.08 cm diameter is encased in either 0.1 cm or 0.4 cm thick steel cylinder. Gap volumes of 5 and 6% for PBXN-109 and C-4, respectively, are located at the outside radius of the HE in the 1D model. The gaps are treated in two different ways in the 2D models. In Model 2Da, either 4% or 5% gap by volume is included at the top end of the cylindrical charge, and a 1% gap is used at the outside radius of the

HE. In Model 2Db, either 5% or 6% gap is included at the top of the cylinder, and there is no gap on the side.

The three heaters were modeled as uniform heat flux surfaces on the tube wall and top and bottom surfaces for the end caps (see Fig. 1). Model Proportional-Integral-Derivative (PID) controllers were used to keep the three control temperatures near their set-point values. Expressions for heat transfer coefficients were applied at all outward facing surfaces of the capped tube to account for the effects of free convection and thermal radiation heat losses to the surroundings [41]. A more refined boundary-layer expression for heat transfer is used at the tube wall to account for spatial variations resulting from the rising warm air. The heat transfer is high near the lower end of the tube wall and decreases up the tube wall as the boundary layer of warm air forms and increases in thickness.

The cookoff simulation starts with a gradual increase of the set-point temperature at location no. 1 in Fig. 1(b) to 130 °C, followed by a hold for 5 hours, and then an increase at a rate of 1 °C/h until cookoff. The upper (no. 2) and lower (no. 3) control thermocouples were kept a few degrees lower than the tube control TC in an effort to place the ignition point in the center of the HE. As the HE is heated, it thermally expands to fill in the gap. At a temperature above 130 °C, exothermic decomposition begins and eventually ignition occurs near the midplane of the system. On a time scale of microseconds, the propagation of flame through the HE causes the temperature and pressure to rise, and ultimately causes a break in confinement.

In the simulations, four different mesh resolutions ($\Delta x, \Delta x/2, \Delta x/4, \Delta x/8$) are considered. In the base case (Δx), there are 12 elements across the HE in the radial direction, and in the fine mesh case there are 96 elements in this direction. The steel vessel has 3 zones across the wall for the base case (Δx), and 24 zones for the $\Delta x/8$ case. The total number of zones is 60000 for the $\Delta x/8$ case. The air/HE interface is not tracked explicitly, and zones with both air and HE have properties determined by the mixing rule discussed next.

C. Numerical strategies for dynamic gaps

In real systems, there are gaps present between the HE sample and its case. Whether the presence of gaps is by design or not, its effect on the cookoff violence is believed to be significant. The ALE3D code has two ways of modeling gaps. The first way uses a

standard sliding contact algorithm that makes use of the concept of master-slave surfaces. Here, finite element boundaries coincide with phase boundaries, and the gap surfaces are explicitly 'tracked.' The second way of treating gaps is the mixed element approach that we use in this work. Interfaces pass through the middle of mixed elements that do not necessarily move with the interface. The interface is resolved on the length scale of this element. Although less accurate, this approach avoids mesh tracking and entanglement problems. The mixed-element approach can provide results of satisfactory accuracy with sufficient mesh resolution.

The mixing rules for mechanical behavior are particularly important for gaps that close. The algorithms of this study were devised with the assumption that the HE/air interface is parallel to the case wall, which is generally valid except at corners of the explosive. Mechanical properties in the mixed zone are weighted in favor of the air in the gap. In the vicinity of this interface, strains normal to the interface are very small for the HE and relatively large for the air in the gap.

D. Time integration method, mass scaling, and transition to burn

The equations of mass, momentum, energy, and chemistry are solved on the long time scale of the heating phase and on the short time scale of the thermal runaway phase in a single simulation. The momentum equation is integrated explicitly during both the slow and fast phases. In order to provide computationally feasible step sizes, the method of variable mass scaling [42] is applied during the slow heating phase. The density is increased in the momentum equation to reduce the sound speed and allow larger step sizes consistent with the Courant condition. However, if the time step size and material density are too large, spurious fluctuations, characteristic of a simple harmonic oscillator, appear. Thus, a tradeoff is required between numerical efficiency and accuracy. In practice, the time step size is fixed during the slow heating phase with the density calculated from the Courant condition. As the mesh is refined, the time-step size is reduced to keep the mass scaling and the sound speed at nearly constant values.

During the transition phase in which the decomposition reactions are accelerating, the time step size is reduced to meet error specifications for the calculation of thermal and composition fields. At the same time, the artificial density is reduced following the Courant

condition until the physical value is obtained. Fig. 8 illustrates the size of time steps during the last three hours before ignition. Plotted on the y-axis are the actual time-step sizes recorded from a standard simulation. As mass is removed from the system, the size of time steps changes from $10^{8}\,\mu$s to $10^{-7}\,\mu$s. An approximate step size decrease on the order of $10^{14}\,\mu$s magnitude is noted during this transition.

When the HE reaches a user-specified temperature at which ignition occurs, the Arrhenius kinetics expression is replaced by a burn model. A level-set method is used in the modeling of the advancing burn front. The equation

$$\phi_t + \boldsymbol{V}(P) \cdot \nabla\phi = 0 \tag{11}$$

keeps track of the front location as the zero level of ϕ. The pressure-dependent burn velocity $\boldsymbol{V}$ is a single valued vector $(V, V, V)^{\top}$. In the most general frame of level sets, ϕ starts out as the signed distance function, is advected by solving Eqn. 11, and then is reinitialized using a distance renormalization procedure discussed by Nichols in [29].

We use the Backward Euler method for the integration of the thermal equations and reaction kinetics during the heating, and transition phases. During the slow heating phase, the time step size is the value selected for the integration of the hydrodynamic equations. A switch is made to an explicit method when the time step size is a user-specified multiple of the Courant time step size calculated with no mass scaling.

V. RESULTS

A. One-dimensional analysis and model verification

The simplified geometry shown in Fig. 7(a) is used to verify the HE models and check for numerical accuracy. Many of the important features of the thermal explosion models can be efficiently explored with quantitative predictions for the time to explosion and qualitative simulations for the vessel wall expansion as described below. Comparisons of model calculations against the experimental records will be described in the two-dimensional analysis section.

The system was heated using the temperature profile described above for control thermocouple no. 1 of Fig. 1(b). The explosive expands radially into the gap, decomposes, and

ignites near the symmetry axis. The ignition temperature based on the control TC no. 2 of Fig. 7(a) is calculated to be 164 °C for C-4 and 163 °C for PBXN-109 (see Table VI). The Δx mesh with 12 zones in the radial direction was used for the calculations. More refined meshes gave the same explosion temperatures to within 1 °C. The 1D result for C-4 compares favorable with the measured STEX value of 168 °C, but there is a significant difference between the 1D value of 163 °C for PBXN-109 and the measured STEX value of 152 °C.

After the ignition, the burn front advances outward into the relatively cold solid explosive. The resulting high pressure product gases drive the steel case outward. Calculated results for the wall hoop strain at location no. 2 of Fig. 7(a) are shown in Figs. 9 and 10 for the one-dimensional STEX model. For comparison, the theoretical thermal expansion of an empty steel vessel is shown in the same plot. The system for C-4 has 6% gap between the HE and the steel plate with thickness of 0.1 cm. For PBXN-109 system, the gap size is 5% and the plate thickness is 0.4 cm. The HE-vessel and empty vessel results should coincide as the temperature increases until the HE expands to fill the vessel or decomposition gases pressurize the vessel. Note that the coefficients of thermal expansion for the explosives are 10X greater than the 4130 steel (see Tables III and IV). The estimated time of contact at which inert HE fills the 5$\sim$6% gap and starts pushing on the steel wall is approximately 53 and 56 hours for PBXN-109 and C-4, respectively. Since the solid HE undergoes chemical decomposition and the decomposition gases pressurize the vessel, the overall strain values are greater than the analytical expansion of the steel vessel alone. The effects of mesh refinement on the strain curves were determined to be negligible during the slow heating phase, since the curves for the coarse (Δx and $\Delta x/2$) and fine ($\Delta x/4$ and $\Delta x/8$) meshes are very similar.

B. Two-dimensional analysis

Two dimensional simulations are performed for the STEX system shown in Figs. 1(b) and 7(b) for C-4 and PBXN-109. This system is assumed to be axisymmetric, and a cylindrical wedge was selected for the calculation domain. In Figs. 11 and 12, calculated temperatures of the STEX system are plotted versus time, along with measured curves. The measured and calculated temperatures are shown at an internal location (no. 6 in Fig. 1(b)) and the control location (no. 1 in Fig. 1(b)). The predicted and measured internal temperature

curves are in good agreement for C-4, and the predicted explosion temperature (TC no. 1) of 167 °C agrees very well with the experimental value of 168 °C (see Table VI). For PBXN-109, the predicted and measured curves for the internal temperature have similar shapes, but the predicted explosion temperature is 160 °C versus 152 °C for the experiment. The differences between the model and measured results are likely the result of inaccuracies in the chemical kinetics models. Despite this discrepancy, both the model and experiment give a lower cookoff temperature for PBXN-109 than C-4. Studies were conducted to assess the accuracy of the calculations and the reproducibility of the measurements. The model simulations were repeated with the refined meshes and are numerically accurate to less than a degree. A replicate STEX test was performed for C-4 (TE-032), and the explosion temperature of 166 °C of this test compares favorably with the value of 168 °C for the test TE-040 presented in this paper. Thus, the model results are numerically accurate and the measurements seem to be reproducible. A question remains as to why the STEX cookoff of PBXN-109 occurs at a temperature of 16 °C less than the 168 °C value for C-4. An inspection of the ODTX curves for the two materials (see Figs. 3 and 4) shows similar results over much of the temperature range. However, at a low temperature of 181 °C, the measured time to explosion is approximately 20,000 s for C-4 versus 4000 s for PBXN-109. These results suggest slower reaction rates for C-4 at low temperatures which helps to account for the higher STEX ignition temperature for C-4.

In Figs. 13 and 14, calculated vessel wall hoop strains for the C-4 and PBXN-10 STEX systems are shown with the measurements over the duration of the tests. As was done for the one-dimensional case, the theoretical expansion of the empty steel vessel is plotted as well. For both explosives, the measured hoop strains agree with the empty-vessel results until a few hours before the ignition point. These results confirm the accuracy of the hoop strain measurements and the polynomial EOS for the 4130 steel. Near the ignition point, decomposition gases pressurize the vessel, and measured strains are greater than the empty-vessel results.

The results for Model 2Da (side gap present) are calculated on meshes of three different resolutions for both C-4 and PBXN-109. In Fig. 15, the calculated wall-hoop strain for C-4 is shown for the base-line case $(\Delta t, \Delta x)$ and a case $(\Delta t/2, \Delta x)$ in which the time-step size is reduced by a factor of two. This decrease in Δt is implemented during the heating phase and reduces the mass scaling. (Note that the value for Δt is not decreased below

the Courant limit.) These simulation results show oscillations, and are generally higher than the measurements and the analytical empty-vessel results. Consequently, calculated pressures within the HE are higher than pressures inferred from strain measurements. Mass scaling and mixed materials modeling of gaps contribute to these artificially high pressures as described below. Near the ignition point there is additional pressurization resulting from the decomposition gases. Note that the deformation of the explosives contributes little to the high pressures since both explosives have low strength and deform easily as they thermally expand and fill the steel vessel. It is seen that the model strains are much higher for C-4 than PBXN-109, particularly near the ignition point. This is due to the thinner steel wall for C-4 (0.1 cm) than PBXN-109 (0.4 cm). The model predicts yielding of the C-4 tube wall before ignition which is not the case for the experiment. This effect is not seen for the PBXN-109 simulations for the 0.4 cm wall. Thus, greater numerical accuracy is needed for lower strength vessels.

As Δx and Δt are reduced, the calculated strain curves are approaching the empty-vessel results. Mesh refinement provides a better representation of the HE/air interface near the vessel wall, and a smaller time-step size decreases the mass scaling. Although the results do not show complete convergence with either the mesh or time-step size, they do provide an approximate description of the mechanical behavior during the heating and ignition phases.

It is useful to further consider the contribution of mass scaling to the numerical artifacts in the calculated strain curves. The large calculated strains are primarily the result of reduced sound speeds from mass scaling. The HE pressurizes the vessel before there is time for the explosive to expand upwards into the gap region near the top of the vessel. If the mass scaling is reduced, the upward expansion occurs faster, there is less pressurization, and the tube wall strains are reduced [43]. The spurious oscillations are similar to those observed for a simple harmonic oscillator in which the motion of the high mass material is guided by the restoring force of material elasticity. As the mass scaling is reduced, the amplitude decreases and the frequency of the oscillations increase. It is important to minimize these errors since the state of the system prior to ignition can have a strong influence on the violence of the expansion.

A rapid expansion of the vessel wall follows the slow heating and ignition phases. In Fig. 16, the wall hoop strain result is compared with the measurement for the PBXN-109 STEX test during the explosive phase. The model result compares favorably with the mea-

sured result until $t = 275\,\mu$s. At this time, the measured strain rate changes dramatically. It is likely that the gauge failed at this point. Just prior to the gauge failure, the measured strain rate is approximately 400 s^{-1}, suggesting relatively low violence consistent with the relatively long time scale of the test.

VI. CONCLUSIONS

A numerical and experimental investigation was performed for the thermally-induced explosion of the RDX-based explosives C-4 and PBXN-109. The explosives were heated in steel vessels at 1 °C/h until reaction. ALE3D models were employed to represent the coupled thermal, chemical, and mechanical behavior through the heating, ignition, and explosive phases. For the solid explosives, we use a polynomial equation of state and an elastic-plastic model. Model parameters were obtained from measurements of thermal and mechanical properties at conditions relevant to both the slow heating and explosive phases of cookoff. All of the gas species are taken to have gamma-law equations of state. Multi-step reaction models are used to represent the chemical kinetics behavior of these materials during the slow heating stage. Model parameters were specified using measurements of the one-dimensional-time to explosion. After ignition, we employ a flame sheet model with a power-law expression for the burn front velocity. Model parameters are determined from measurements of burn velocity in strands of explosive. During the heating phase, an implicit method is employed for the integration of the thermal-chemical transport equations, and an explicit method with mass scaling is used for the hydrodynamic equations. A mixed materials method was used to model the gap between the HE and vessel wall, while a level-set method was utilized to model the propagation of the burn front.

Calculations for one-dimensional models of the thermal explosion experiments for C-4 and PBXN-109 provide useful estimates for the explosion temperature. They also provide an approximate model for the wall expansion, and an assessment of numerical accuracy. Two-dimensional calculations for the temperature fields and explosion temperature are in good agreement with thermocouple measurements for C-4, but there are larger differences between predicted and experimental results for PBXN-109. The ALE3D models provide an approximate representation of wall motion during the heating phase. Calculated strains exhibit oscillatory behavior and are larger than the measured values due to artificial pressure

rises from mass scaling. This effect is larger for the thin wall tube (0.1 cm) of the C-4 experiment than the thick wall tube of the PBXN-109 test. The ALE3D model provides an excellent representation for the wall motion during the explosive phase for PBXN-109. In the future, an implicit hydro method will be employed to provide more accurate mechanical results during the heating phase. This improved numerical accuracy is needed since the mechanical state of the system at ignition can strongly influence violence.

Acknowledgments

The work was performed under the auspices of the U.S. Department of Energy by the University of California, Lawrence Livermore National Laboratory under Contract No. W-7405-Eng-48.

Authors would like to thank Albert Nichols for developing the ALE3D chemistry capability needed for the thermal explosion simulation.

---

[1] Mair, H. U., 'Review: Hydrocodes for Structural Response to Underwater Explosions,' *Shock and Vibration*, **6**, pp. 81–96, 1999.

[2] McGlaun, J. M., and Yarrington, P., Asay, J. R., and Shahinpoor, M., (Eds.) High Pressure Shock Compression of Solids, *Large Deformation Wave Codes*, Springer-Verlag, 1993.

[3] Anderson, Jr., C. E., 'An Overview of the Theory of Hydrocodes,' *Int. J. Impact Engineering*, **5**, pp. 33–59, 1987.

[4] McGlaun, J. M., Thompson, S. L., and Elrick, M. G., 'CTH: a Three-dimensional Shock Wave Physics Code,' *Int. J. Impact Engineering*, **10**, pp. 351–360, 1990.

[5] Mandell, D. A., Adams, T. F., Mosso, S. J., Holian, K. S., Addessio, F. L., and Baumgardner, J. R., 'MESA: a 3-D Computer Code for Armor/Anti-Armor Applications,' Los Alamos National Laboratory, Report LA-UR-89-1263, 1989.

[6] Quirk, J. J., 'A Parallel Adaptive Grid Algorithm for Computational Shock Hydrodynamics,' *Applied Numerical Mathematics*, **20**, pp. 427–453, 1996.

[7] Yao, J., and Stewart, D. S., 'On the Dynamics of Multidimensional Detonation,' *J. Fluid Mechanics*, **309**, pp. 225–275, 1996.

[8] Stewart, D. S., Aslam, T., Yao, J., and Bdzil, J. B., 'Level-set Techniques Applied to Unsteady Detonation Propagation,' *Modeling in Combustion Science, Proceedings, Springer-Verlag*, pp. 352–369, Berlin, Germany, 1995.

[9] Bourlioux, A., and Majda, A. J., 'Theoretical and Numerical Structure for Unstable Two-Dimensional Detonations,' *Combustion and Flame*, **90**, pp. 211–229, 1992.

[10] Oran, E. S., Boris, J. P., Young, T., Flanigan, M., Burks, T., and Picone, M., 'Numerical Simulations of Detonations in Hydrogen-Air and Methane-Air Mixtures,' *Proceedings of 18th Symposium on Combustion*, The Combustion Institute, 1981, pp. 1641–1649.

[11] McClelland, M. A., Maienschein, J. L., Nichols, A. L., Wardell, J. F., Atwood, A. I., and Curran, P. O., 'ALE3D Model Predictions and Materials Characterization for the Cookoff Response of PBXN-109,' *Proceedings of JANNAF 38th Combustion and 20th Propulsion Systems Hazards Subcommittee Meetings*, Destin, FL, 2002.

[12] McClelland, M. A., Tran, T. D., Cunningham, B. J., Weese, R. K., and Maienschein, J. L., 'Cookoff Response of PBXN-109: Material Characterization and ALE3D Thermal Predictions,' *Proceedings of JANNAF 50th Propulsion Meeting*, Salt Lake City, UT, 2001.

[13] McClelland, M. A., Maienschein, J. L., Nichols, A. L., and Yoh, J. J., 'Ignition and Initiation Phenomena: Cookoff Violence Prediction,' *Joint DoD/DOE Munitions Technology Development Program FY-02 Report*, UCRL-ID-103482-02, 2002.

[14] Wardell, J. F., and Maienschein, J. L., 'The Scaled Thermal Explosion Experiment,' in *Proceedings of 12th International Detonation Symposium*, San Diego, CA, Office of Naval Research, 2002.

[15] Nichols, A. L., Couch, R., McCallen, R. C., Otero, I., and Sharp, R., 'Modeling Thermally Driven Energetic Response of High Explosives,' *Proceedings of 11th International Detonation Symposium*, Snowmass, Colorado, pp. 862–871, 1998

[16] Yoh, J. J., and McClelland, M. A., 'Simulating the Thermal Response of High Explosives on Time Scales of Days to Microseconds,' *Proceedings of 13th APS SCCM Conference*, Portland, Oregon, 2003.

[17] Yoh, J. J., McClelland, M. A., Maienschein, J. L., Nichols, A. L., and Wardell, J. F., 'Towards an Ideal Cookoff Model for PBXN-109,' *Proceedings of JANNAF 21st Propulsion Systems Hazards Subcommittee Meetings*, Colorado Springs, Colorado, 2003.

[18] Yoh, J. J., McClelland, M. A., Maienschein, and Wardell, J. F., 'Towards a Predictive Thermal Explosion Model for Energetic Materials,' *J. of Computer-Aided Materials Design*, in press, 2004.

[19] Chidester, S. K., Tarver, C. M., Green, L. G., and Urtiew, P. A., 'On the Violence of Thermal Explosion in Solid Explosives,' *Combustion and Flame*, **110**, pp. 264–280, 1997.

[20] Tarver, C. M., and Tran, T. D., 'Thermal Decomposition Models for HMX-based Plastic Bonded Explosives,' *Combustion and Flame*, **137**, pp50–62, 2004.

[21] Baer, M. R., Hobbs, M. L., Gross, R. J., and Schmitt, R. G., 'Cookoff of Energetic Materials,' *Proceedings of 11th International Detonation Symposium*, Snowmass, Colorado, Office of Naval Research, pp. 852–861, 1998.

[22] Matheson, E. R., Drumheller, D. S., and Baer, M. R., 'A Coupled Damage and Reaction Model for Simulating Energetic Material Response to Impact Hazards,' *Proceedings of APS SCCM Conference*, Snowbird, Utah, pp. 651–654, 1999.

[23] Schmitt, R. G., Erikson, W. W., Away, B., Dickson, P., Henson, B., Smilowitz, L., and Tellier, L., 'Application of a Multiphase Mixture Theory with Coupled Damage and Reaction to the LANL Large-Scale Annular Cookoff Experiment,' *Proceedings of JANNAF 19th Propulsion Systems Hazards Subcommittee Meetings*, Monterey, CA., 2000.

[24] Atwood, A. I., Curran, P. D., Lee, K. B., and Bui, D. T., 'Experimental Progress on a Cookoff Model Validation Effort,' *Proceedings of JANNAF 38th Combustion and 20th Propulsion Systems Hazards Subcommittee Meetings*, Destin, FL, 2002.

[25] Sandusky, H. W., and Chambers, G. P., 'Validation Experiments for Slow Cookoff,' *Proceedings of JANNAF 38th Combustion and 20th Propulsion Systems Hazards Subcommittee Meetings*, Destin, FL, 2002.

[26] Erikson, W. W., and Schmitt, R. G., 'Pre- and Post-ignition Modeling of Validation Cookoff Experiments,' *Proceedings of JANNAF 38th Combustion and 20th Propulsion Systems Hazards Subcommittee Meetings*, Destin, FL, 2002.

[27] Meyer, R., Kohler, J., and Homburg, A, *Explosives*, Wiley-VCH, New York, 1993.

[28] Belytschko, T., 'An Overview of Semidiscretization and Time Integration Procedures,' in *Computational Methods for Transient Analysis*, edited by T. Belytschko and T. J. R. Hughes, North-Holland, 1983, pp. 1–65.

[29] Sharp, R., and the ALE3D Team, *Users Manual for ALE3D*, Lawrence Livermore National Laboratory, Ver. 3.6.1, October 25, 2003.

[30] McGuire, R. R., and Tarver, C. M., 'Chemical Decomposition Models for the Thermal Explosion of Confined HMX, TATB, RDX, and TNT Explosives,' *Proceedings of 7th International Detonation Symposium*, Annapolis, MD, Naval Surface Weapons Center, 1981, pp. 56–64.

[31] Steinberg, D. J., 'Equation of State and Strength Properties of Selected Materials,' UCRL-MA-106439, 1991.

[32] Catalano, E., McGuire, R., Lee, E. L., Wrenn, E., Ornellas, D., and Walton, J., 'The Thermal Decomposition and Reaction of Confined Explosives,' *Proceedings of 6th International Detonation Symposium*, Coronado, CA, Office of Naval Research, pp. 214–222, 1976.

[33] Tran, T. D., 'A Compilation of One-Dimensional, Time-To-Explosion (ODTX) Test Data for High Explosives and Propellants,' UCRL-ID-151449, 2003.

[34] Maienschein, J. L., and Wardell, J. F., 'Deflagration Rate of PBXN-109 and Composition B at High Pressures,' *Proceedings of JANNAF 38th Combustion and 20th Propulsion Systems Hazards Subcommittee Meetings*, Destin, FL, 2002.

[35] McClelland, M. A., Maienschein, J. L., and Nichols, A. L., 'Ignition and Initiation Phenomena: Cookoff Violence Prediction,' *Joint DoD/DOE Munitions Technology Development Program FY-01 Report*, UCRL-ID-103482-01, 2001.

[36] Fried, L. E., and Howard, W. M., *Cheetah 3.0 Users Manual*, Lawrence Livermore National Laboratory, Livermore, CA, UCRL-MA-117541, 2001

[37] Steinberg, D. J., Cochran, S. G., and Guinan, M. W., 'A Constitutive Model for Metals Applicable at High-strain Rate,' *Journal of Applied Physics*, **51**, pp. 1498–1504, 1980.

[38] Royce, E. B., 'GRAY, a Three-Phase Equation of State for Metals,' Lawrence Livermore National Laboratory, Livermore, CA, UCRL-51121, 1971

TABLE I: Chemical kinetics parameters for decomposition of C-4.

Reaction step	$\ln Z_k$	E_k (kJ/g-mole-^{o}K)	q_k (J/g)
A $\rightarrow$ B	43.70 s^{-1}	197.2	139.0 (endothermic)
B $\rightarrow$ C	38.90 s^{-1}	184.7	-535.6 (exothermic)
C $\rightarrow$ D	32.69 cm^3/s-g	142.8	-4680 (exothermic)

TABLE II: Chemical kinetics parameters for decomposition of PBXN-109 ($\bar{\text{C}}$ = C + *Al*).

Reaction step	$\ln Z_k$	E_k (kJ/g-mole-^{o}K)	q_k (J/g)
A $\rightarrow$ B	43.84 s^{-1}	194.7	268.0 (endothermic)
B $\rightarrow \bar{\text{C}}$	39.04 s^{-1}	182.5	-803.9 (exothermic)
C $\rightarrow$ D	32.84 cm^3/s-g	141.1	-4241.2 (exothermic)

[39] Gust, W. H., 'High Impact Deformation of Metal Cylinders at Elevated Temperatures,' *Journal of Applied Physics*, **53**, pp. 3568–3575, 1982.

[40] Bird, R. B., Stewart, W. E., and Lightfoot, E. N., *Transport Phenomena*, John Wiley & Sons, Inc., 1960, pp. 260–261.

[41] Holman, J. P., *Heat Transfer*, McGraw-Hill, 1976, pp. 253–254.

[42] Prior, A. M., 'Applications of Implicit and Explicit Finite Element Techniques to Metal Forming,' *J. of Material Processing Technology*, **45**, pp. 649–656, 1994.

[43] McClelland, M. A., Maienschein, J. L., Reaugh, J. E., Tran, T. D., Nichols, A. L., and Wardell, J. F., 'ALE3D Model Predictions and Experimental Analysis of the Cookoff Response of Comp B,' *Proceedings of JANNAF 21st Propulsion Systems Hazards Subcommittee Meetings*, Colorado Springs, Colorado, 2003.

TABLE III: Constitutive parameters of C-4 and PBXN-109.

Parameter	Units	C-4		PBXN-109	
		Solids	Gases	Solids	Gases
Density, ρ_0	kg/m^3	1670[a]	1670	1670[b]	1670
Coeff. 7-term polynomial, a_0	GPa	0		0	
Bulk modulus, a_1	GPa	2.19		2.82[c]	
Coeff. 7-term polynomial, a_2	GPa	74.2		17.3	
Coeff. 7-term polynomial, a_3	GPa	0		144	
Coeff. 7-term polynomial, b_0		0.344		0.461	
Coeff. 7-term polynomial, b_1		0.344		0.461	
Coeff. 7-term polynomial, b_2		0		0	
Thermal conductivity, k	W/m/^{o}C	0.260[a]	0.219[d]	0.454[a]	0.079[e]
Specific heat, c_v	J/kg/^{o}C	1048[f]	2160[g]	1330[f]	1960[g]
Thermal expansion coeff., α	^{o}C^{-1}	1.04×10^{-4}[h]		1.21×10^{-4}[h]	
Initial shear modulus, μ_0	GPa	1.0×10^{-3}[i]		4.628×10^{-3}[c]	
Initial yield strength, Y_0	GPa	1.0×10^{-4}[i]		6.0×10^{-2}[c]	
Gamma-law coefficient, γ			1.299[j]		1.279[j]

[a]Based on LLNL Handbook at (T,P)=(20 ^{o}C, 1 atm).

[b]Atwood *et al.*, JANNAF 19th Propulsion Systems Hazards Subcommittee Meetings, Monterey, CA., 2000.

[c]Measured at LLNL.

[d]Bridgmann at (T,P)=(20 ^{o}C, 986.9 atm). Note temperature dependence.

[e]Bridgmann at (T,P)=(400 ^{o}C, 986.9 atm). Note temperature dependence.

[f]$c_v = \frac{c_p}{1+T_0(3\alpha)^2 v_s}$; v_s, sound speed based on Navy Handbook, $T_0 = 20\,^o$C.

[g]Calculated from Cheetah at (T,P)=(20 ^{o}C, 986.9 atm).

[h]$\alpha = \frac{b_0 \rho_0 c_v}{3a_1}$.

[i]Modeled.

[j]Fit to match EOS at (2000 ^{o}C, 986.9 atm).

TABLE IV: Constitutive parameters of 4130 Steel and air.

Parameter	Units	4130 Steel	Air (Void Gas)
Density, ρ	kg/m^3	7830	1.206
Coeff. 7-term polynomial, a_0	GPa	0	
Bulk modulus, a_1	GPa	159	
Coeff. 7-term polynomial, a_2	GPa	160	
Coeff. 7-term polynomial, a_3	GPa	0	
Coeff. 7-term polynomial, b_0		1.65	
Coeff. 7-term polynomial, b_1		0.5	
Coeff. 7-term polynomial, b_2		0	
Thermal conductivity, k	W/m/ ^{o}C	42.7	0.0257[a]
Specific heat, c_v	J/kg/ ^{o}C	444	707
Thermal expansion coeff., α	^{o}C^{-1}	1.21×10^{-5}[b]	
Initial shear modulus, μ_0	GPa	77	1.0×10^{-3}[c]
Initial yield strength, Y_0	GPa	1.03	1.0×10^{-4}[c]
Gamma-law coefficient, γ			1.4

[a](T,P)=(20 ^{o}C, 1 atm).
[b]$\alpha = \frac{b_0 \rho_0 c_v}{3a_1}$.
[c]Modeled quantity for air gaps.

TABLE V: Constants in the equations of shear modulus and yield stress.

Material	μ_0 (Mbar)	Y_0 (Mbar)	$Y_{\max}$ (Mbar)	β	n	b (Mbar^{-1})	h (K^{-1})	Comments
C-4	4.628e-05	6.0e-4						
PBXN-109	4.628e-05	6.0e-4	6.1e-04	0.1	1.0	0.0	2.34e-03	
Steel 4130	0.770	1.0300E-02	0.031	125	0.070	0.0	5.0505E-04	

TABLE VI: Comparison of explosion temperatures.

Material	Experiment	Simulation	
		1D	2D
C-4	168 °C	164 °C	167 °C
PBXN-109	152 °C	163 °C	160 °C

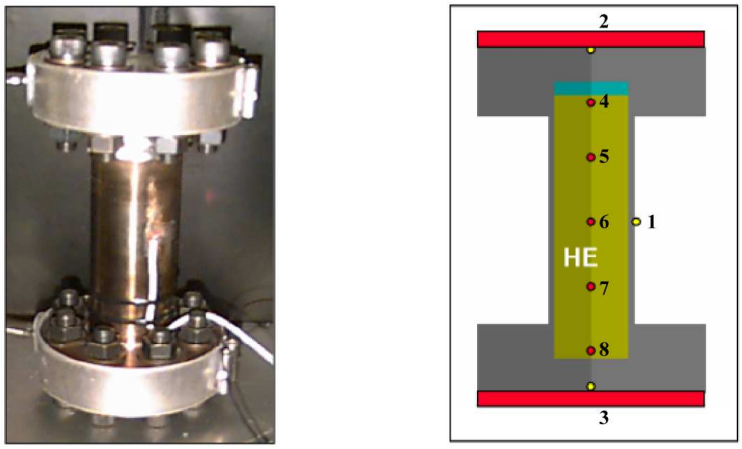

FIG. 1: (a) Photograph of the STEX vessel. (b) Schematic of the ALE3D model domain.

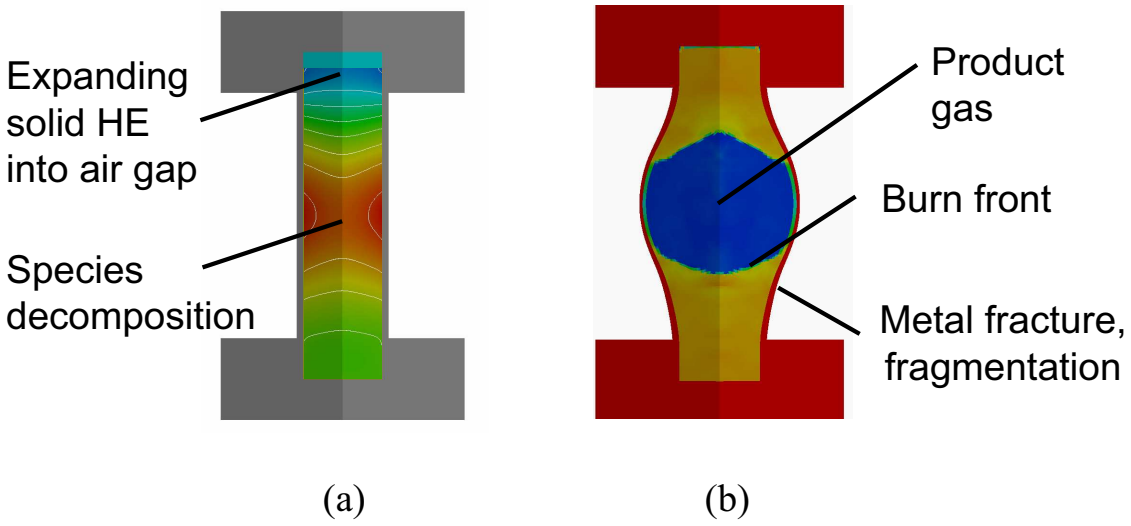

FIG. 2: (a) Pre-ignition characterized by slow thermo-chemical decomposition of HE. (b) Post-ignition illustrated with rapid burn propagation due to expanding hot product gases.

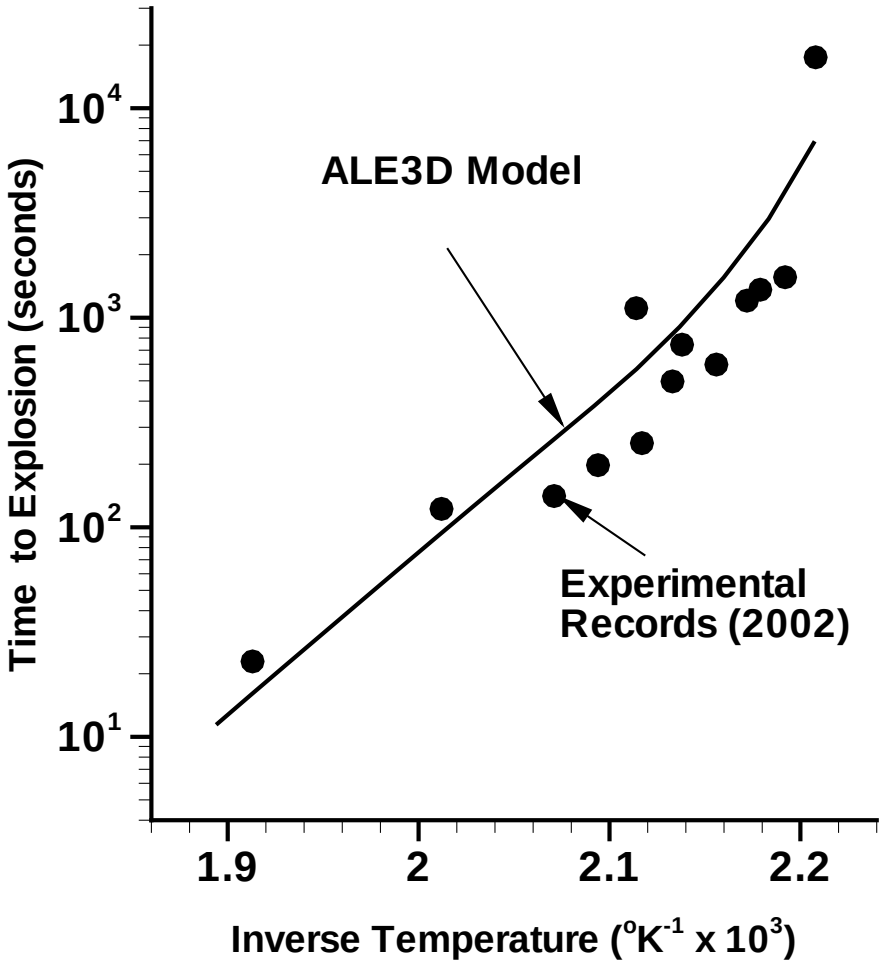

FIG. 3: Experimental and calculated ODTX times to thermal explosion versus inverse temperature for C-4.

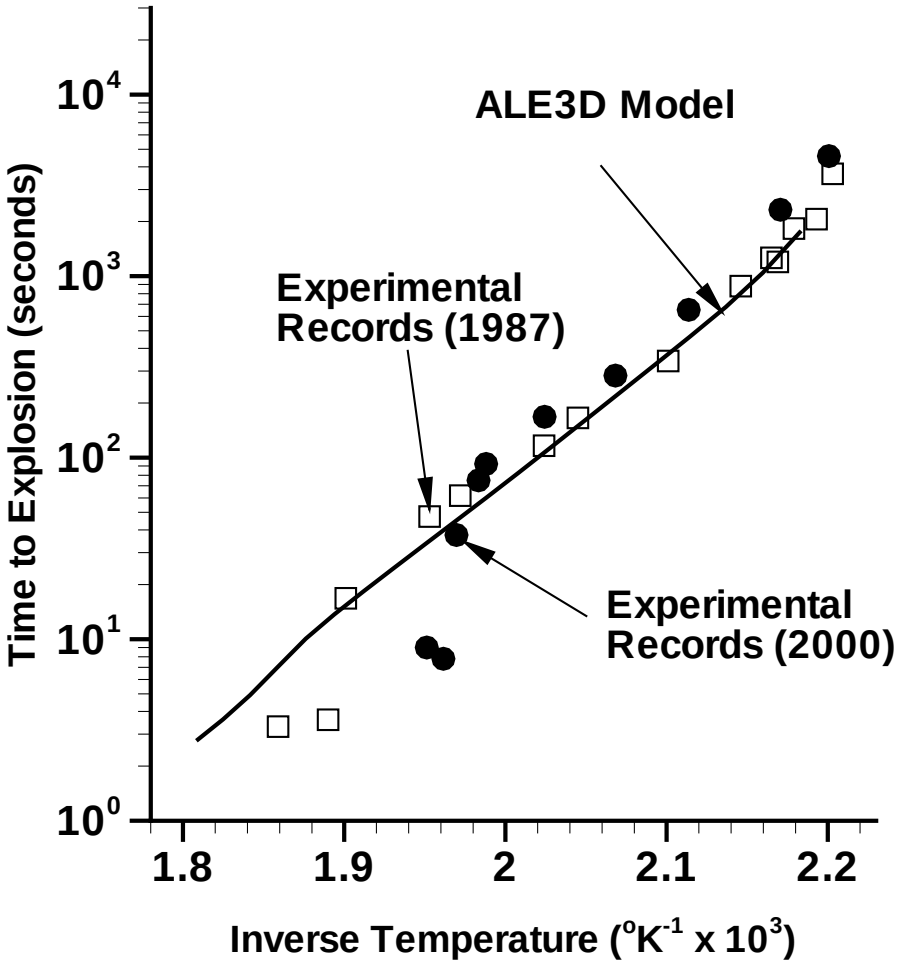

FIG. 4: Experimental and calculated ODTX times to thermal explosion versus inverse temperature for PBXN-109.

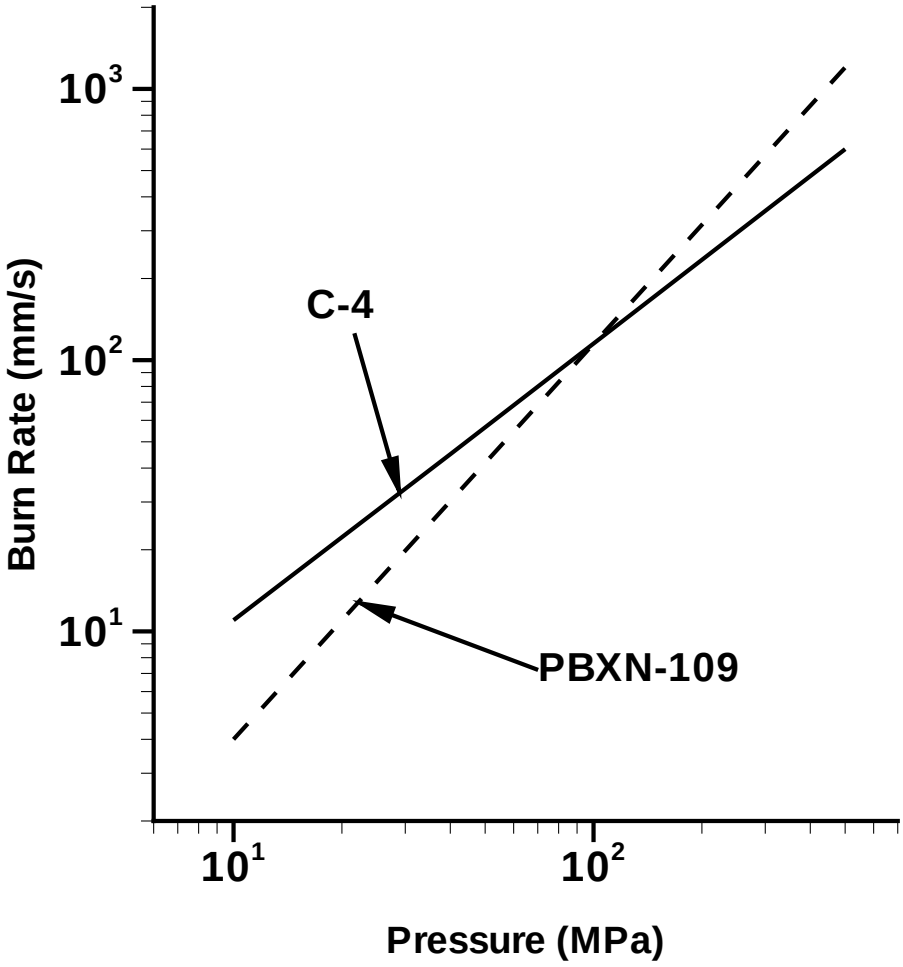

FIG. 5: Curve fits of the measured rate of deflagration for both HE's.

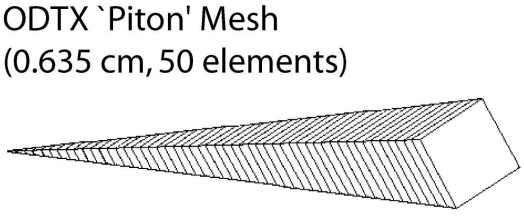

FIG. 6: One-dimensional (spherical symmetry) mesh used in the ODTX simulations.

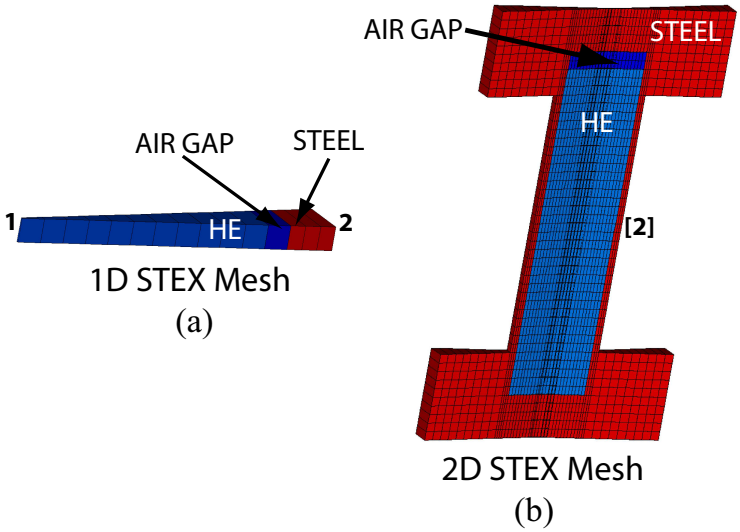

FIG. 7: Meshes used in the STEX simulation. The 1D mesh is generated from a slice along the center radial line of the 2D mesh on the right. The steel wall thickness is 0.1 cm for C-4 (not shown), and 0.4 cm for PBXN-109. In both, there exists a 6% gap (by volume) in C-4 system while a 5% gap is present in the PBXN-109 system.

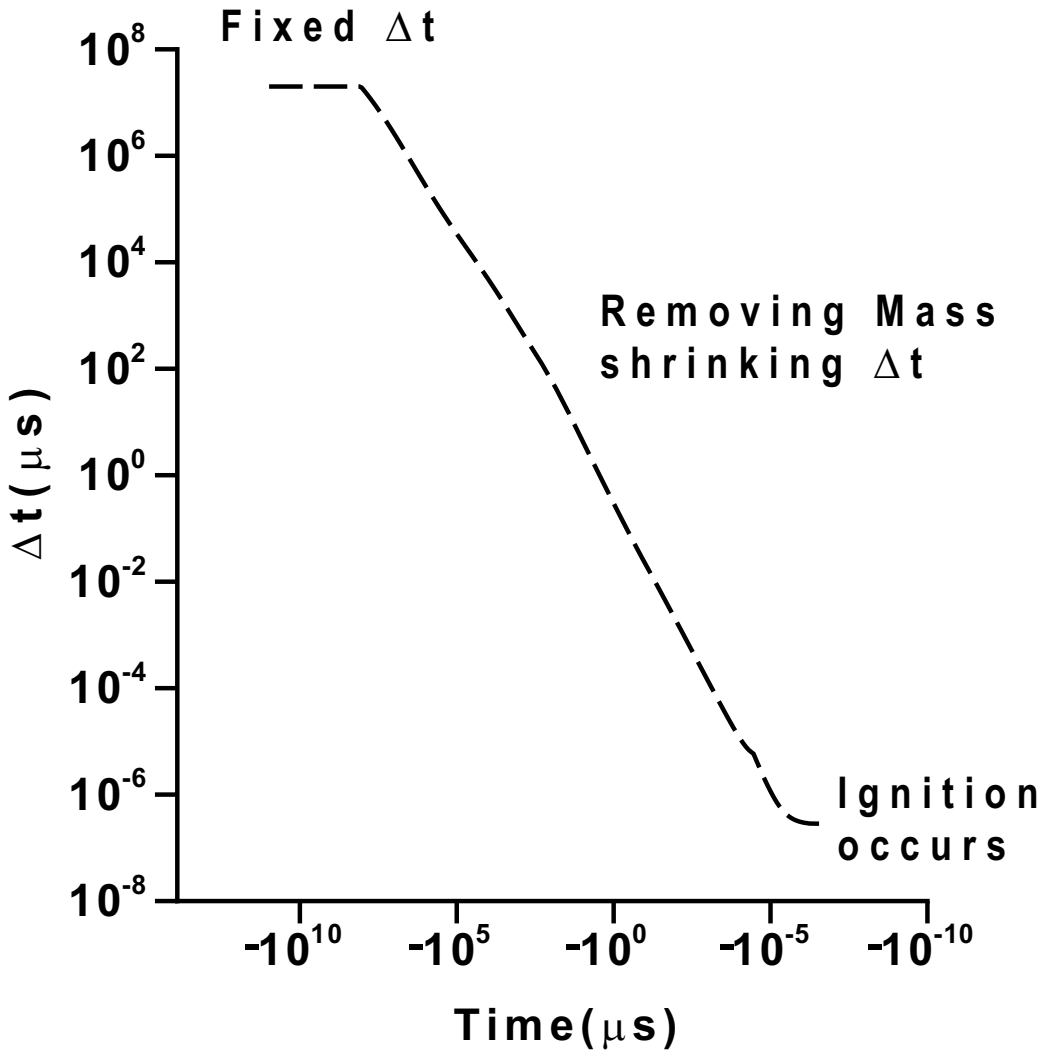

FIG. 8: History of the time-step size during the final hours of thermal explosion. Shown from 3 hours prior to ignition at time $t \approx 10^{-7}$ μs.

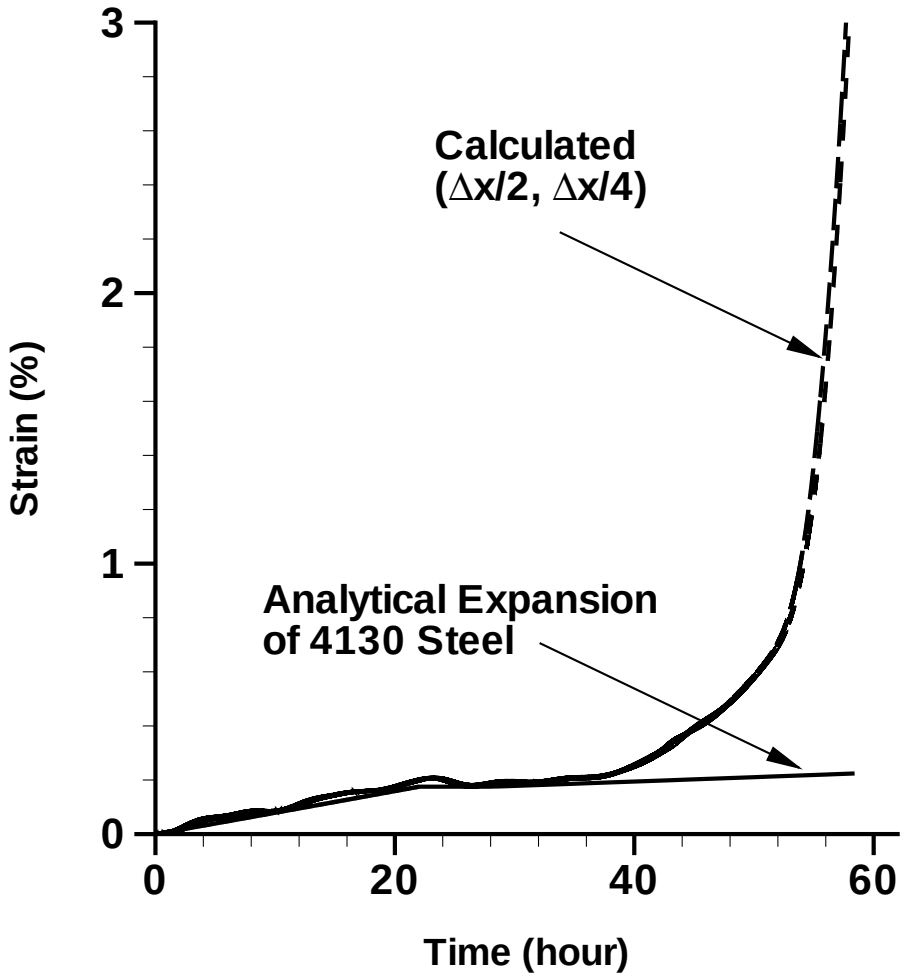

FIG. 9: Simulated mechanical repsonse of confined C-4 in a 1D STEX model. The wall hoop strain is at location no. 2 in Fig. 7(a). The strain calculation agrees with the empty vessel result until about 40 hours as chemical decomposition of HE becomes pronounced in the confined system.

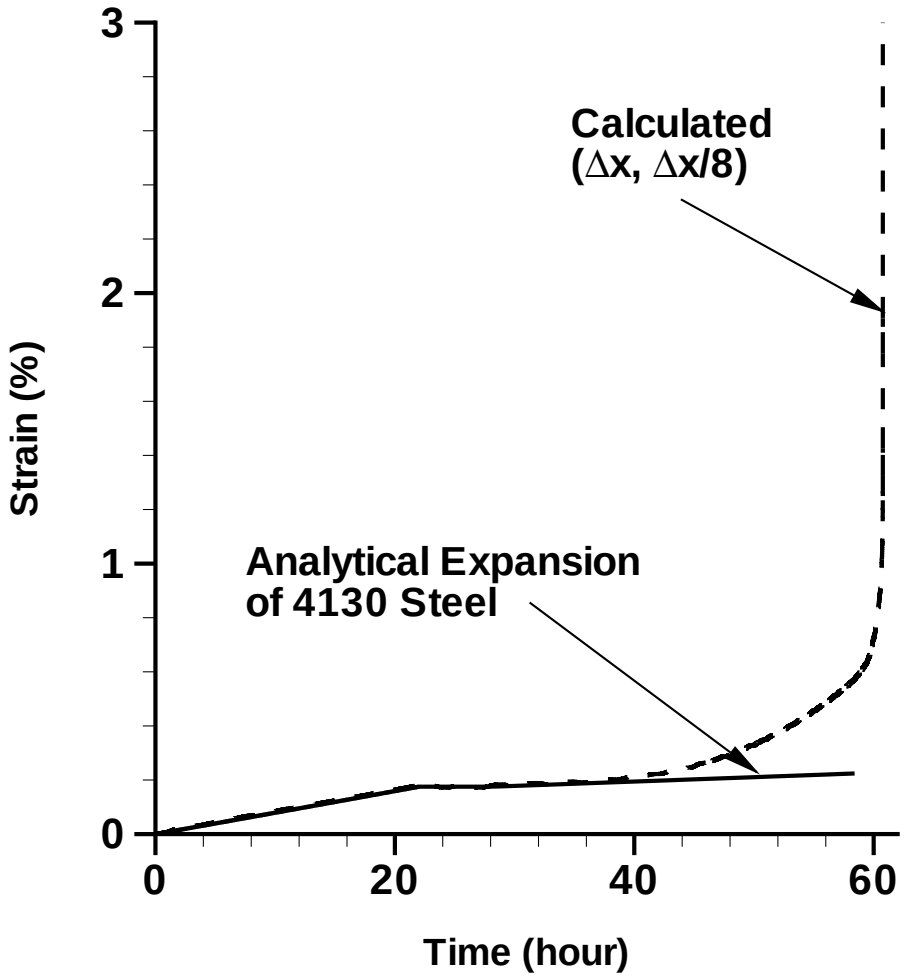

FIG. 10: Simulated mechanical repsonse of confined PBXN-109 in a 1D STEX model. The wall hoop strain is at location no. 2 in Fig. 7(a). The strain calculation agrees with the empty vessel result until about 40 hours as chemical decomposition of HE becomes pronounced in the confined system.

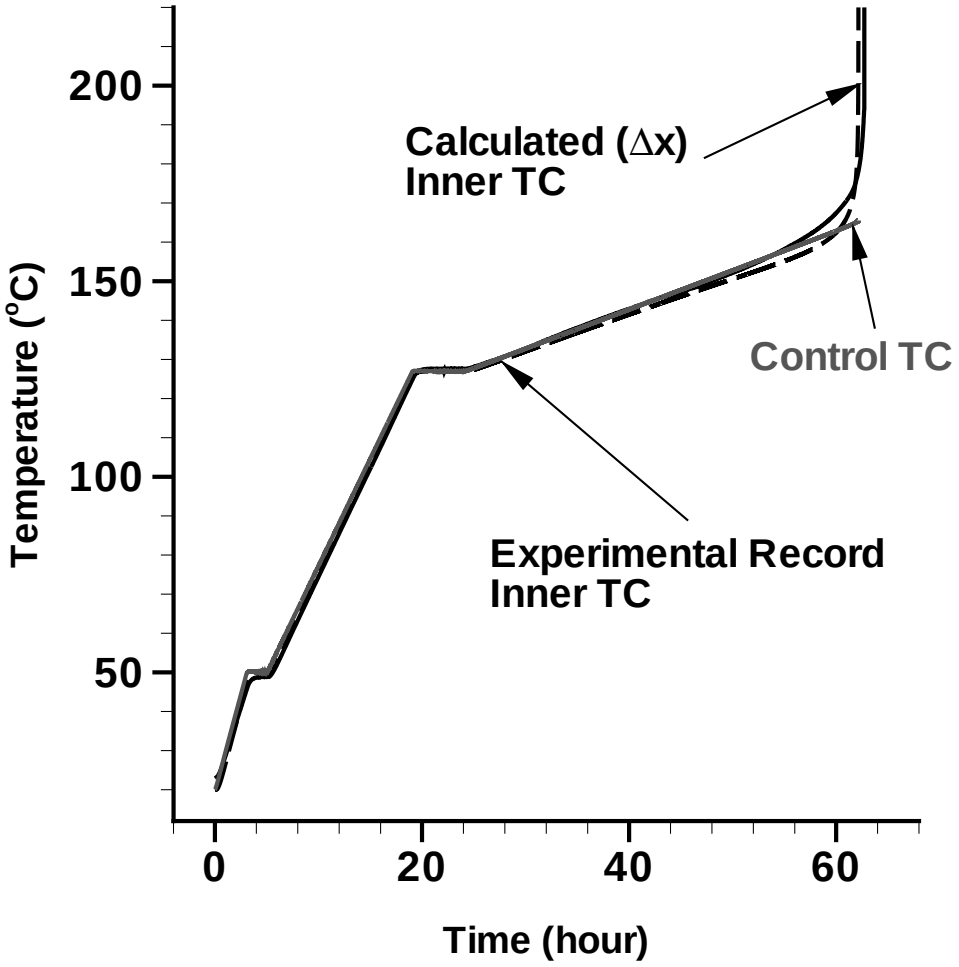

FIG. 11: Calculated thermal response of confined C-4 in a 2D STEX experiment. The control and internal thermocouples are located at positions nos. 1 and 6 in Fig. 1(b), respectively. The predicted ignition temperature is approximately 1 degree lower than the STEX result. Δx mesh is used.

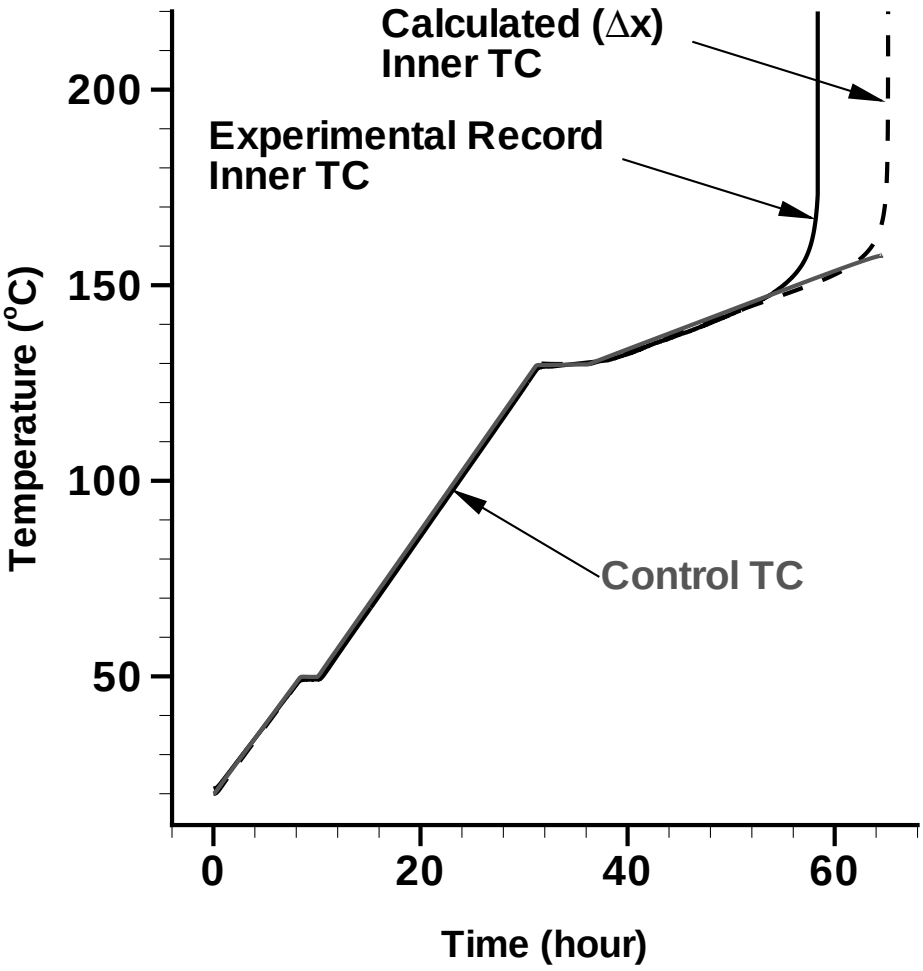

FIG. 12: Calculated thermal response of confined PBXN-109 in a 2D STEX experiment. The control and internal thermocouples are located at positions nos. 1 and 6 in Fig. 1(b), respectively. The predicted ignition temperature is 8 degrees higher than the STEX result. Δx mesh is used.

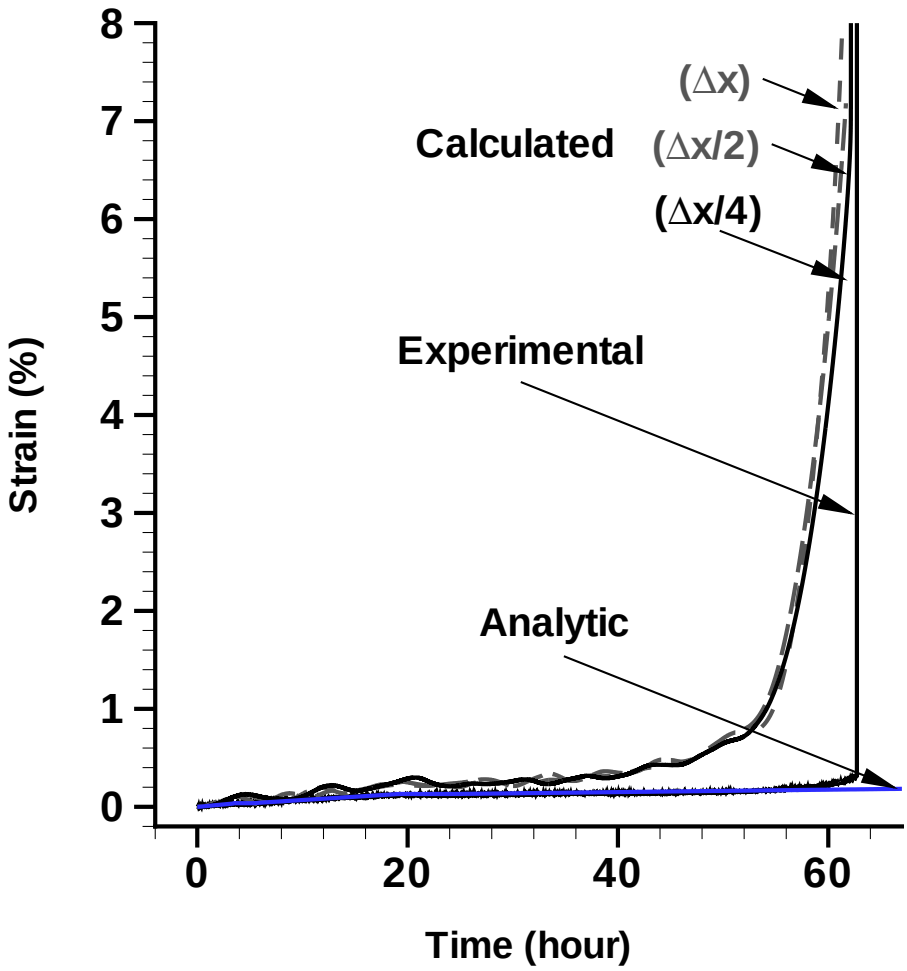

FIG. 13: Experimental and calculated hoop strain records from the slow heating to the thermal runaway phase for C-4.

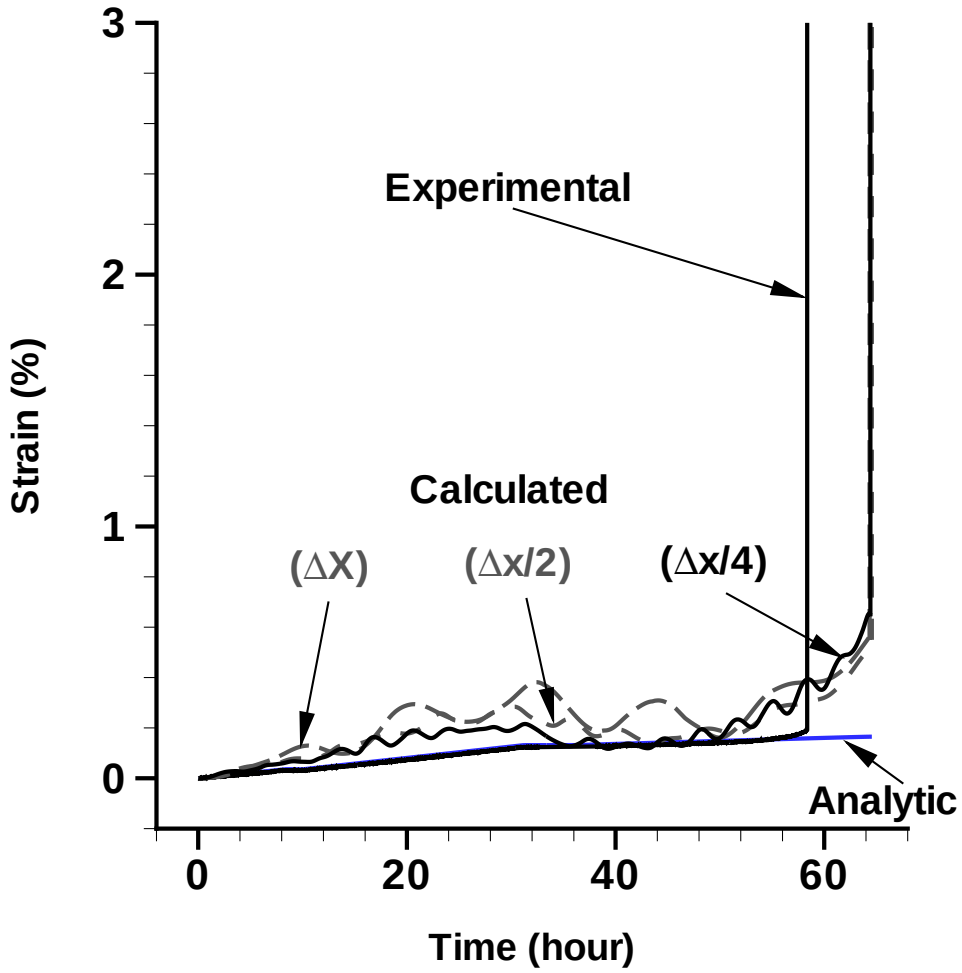

FIG. 14: Experimental and calculated hoop strain records from the slow heating to the thermal runaway phase for PBXN-109.

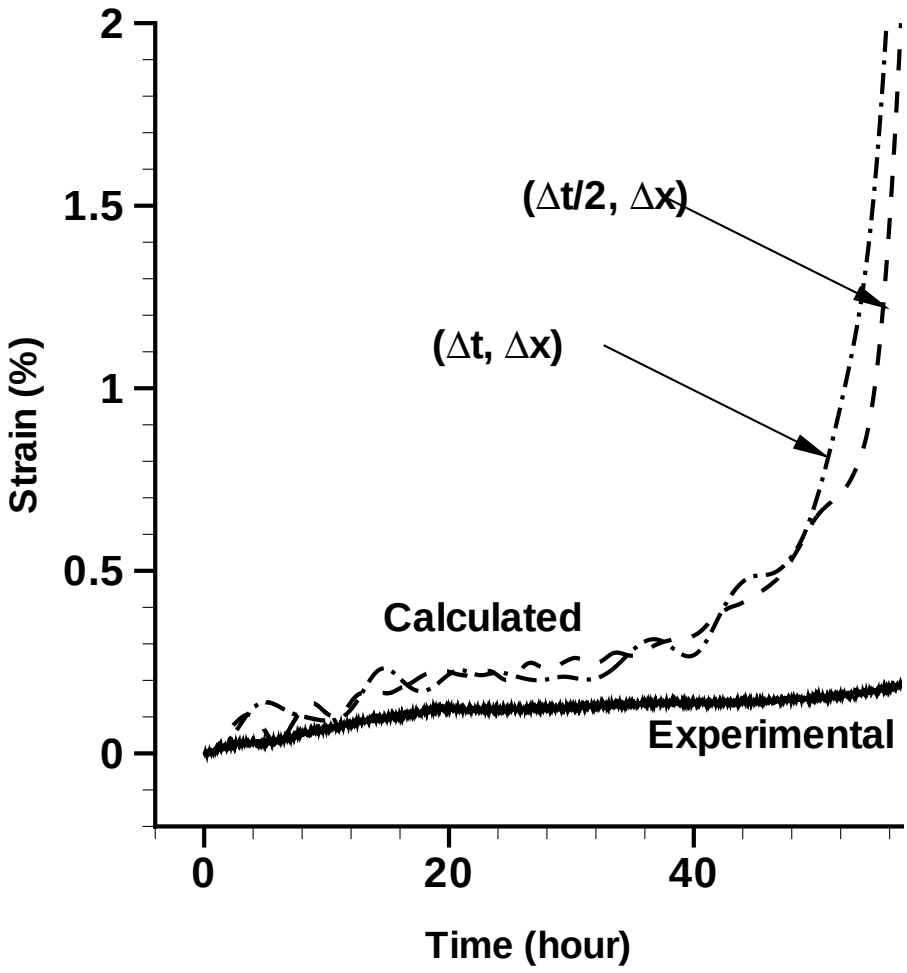

FIG. 15: The effect of mass scaling refinement shown in thin-walled vessel test for C-4.

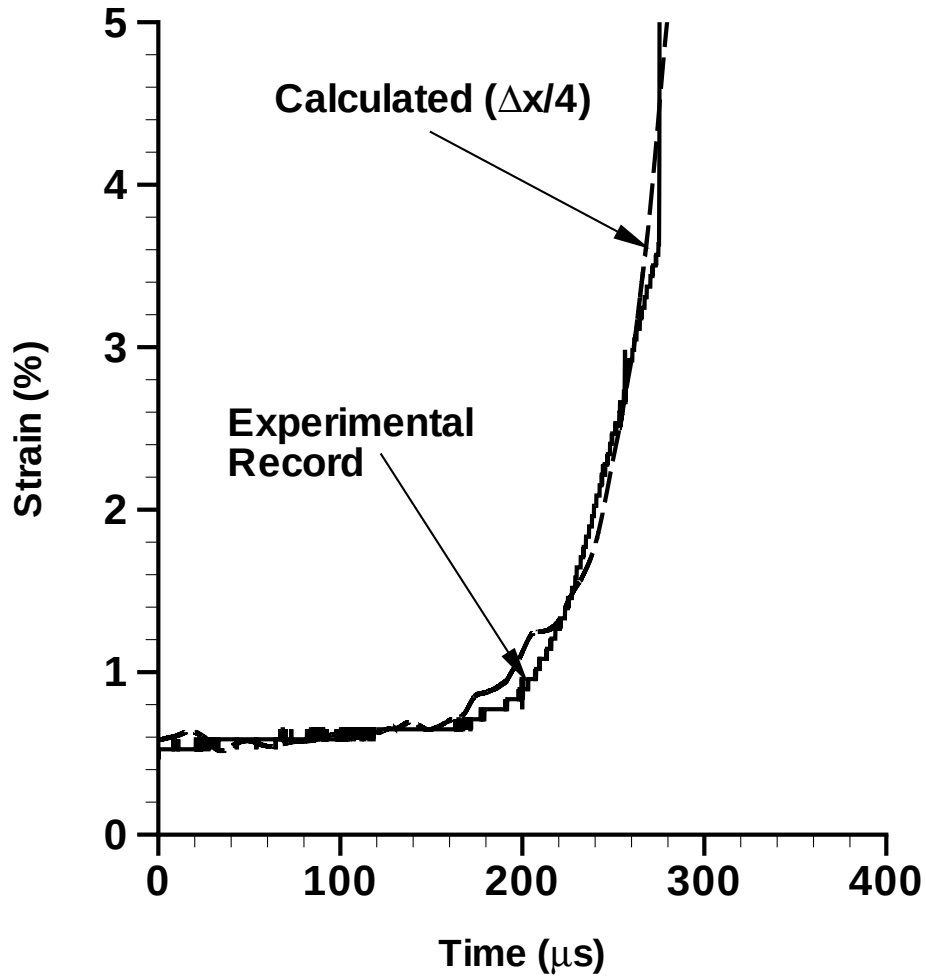

FIG. 16: Experimental and calculated hoop strain records during the rapid explosive phase for PBXN-109.